



Title	Aseismic slip during the 1996 earthquake swarm in and around the Onikobe geothermal area, NE Japan
Author(s)	Takada, Youichiro; Furuya, Masato
Citation	Earth and Planetary Science Letters, 290(3-4), 302-310 <a href="https://doi.org/10.1016/j.epsl.2009.12.024">https://doi.org/10.1016/j.epsl.2009.12.024</a>
Issue Date	2010-02-20
Doc URL	<a href="http://hdl.handle.net/2115/42809">http://hdl.handle.net/2115/42809</a>
Type	article (author version)
File Information	EPSL290-3-4_302-310.pdf



[Instructions for use](#)

# Aseismic Slip during the 1996 Earthquake Swarm in and around the Onikobe Geothermal Area, NE Japan

Youichiro Takada\* Masato Furuya<sup>1</sup>

*Department of Natural History Sciences, Hokkaido University, N10W8, Kita,  
Sapporo 060-0810, JAPAN.*

---

## **Abstract**

In August 1996, an earthquake swarm including 4 earthquakes of magnitudes greater than 5 occurred in and around the Onikobe geothermal area, northeast Japan. While earlier studies detected ground displacements by L-band JERS radar interferograms, there remained certain puzzling discrepancies between the observations and the predictions from a seismologically inferred model, and no satisfactory models have yet been proposed. Here, by identifying that a steep gradient in the radar line-of-sight changes exists in seismicity gaps to the east and west of the Torage area (just to the north of the Onikobe caldera), we propose two aseismic reverse faults, which turn out to contribute to a local topographic growth as well as explaining the pre-existing discrepancies. Another significant signal is detected in a region in which no large earthquakes occurred; we account for this signal by another aseismic fault. This fault adds to another evidence for the recent hypothesis that aseismic fault motion drives earthquake swarm.

*Key words:* Aseismic Slip, InSAR, Earthquake Swarm, Topographic Growth, Onikobe Caldera

*Preprint submitted to Earth and Planetary Science Letters*

---

## 1 Introduction

The Onikobe area in the backbone range running through NE Japan is one of the most active geothermal areas in Japan (Fig. 1) and has been experiencing M5-class earthquakes roughly every 10 years (Umino et al., 1998; Nakajima and Hasegawa, 2003). Four earthquakes of  $M \geq 5.0$  occurred in and around the Onikobe caldera on 11 and 13 August 1996; these earthquakes accompanied over 1700 earthquakes of  $M > 1$  by the end of September (Japan Meteorological Agency (JMA), Fig. 1), and thus we may regard the entire earthquake sequences as a swarm event. Fig.2 shows the focal mechanisms of major earthquakes determined by Umino et al. (1998), including previous earthquakes in 1970s and 1980s. This area is characterized by very complex rock types (mainly volcanic), and densely distributed faults as evidenced by those earthquake mechanisms (Fig.2); it should also be noted that none of those faults were exposed on the surface. While earthquake fault models were estimated for those large earthquakes from seismic data (Umino et al., 1998; Okada et al., 2001) and previous studies had already reported a detection of associated ground displacements by Interferometric Synthetic Aperture Radar (InSAR) (Aoki et al., 2002; Yagai et al., 2002), the ground displacement pre-

\* Corresponding author; Now at Institute for Research on Earth Evolution (IFREE), Japan Agency for Marine-Earth Science and Technology (JAMSTEC). 3173-25 Showa-machi, Kanazawa-ku, Yokohama 236-0001, Japan. ytakada@jamstec.go.jp (Youichiro Takada), Tel.: +81-45-778-5965, Fax.: +81-45-778-5439

<sup>1</sup> furuya@mail.sci.hokudai.ac.jp (Masato Furuya)

19 dicted from the seismologically derived fault models did not fit the observed  
20 InSAR data as we discuss in Section 2.

21 Here we propose a new fault model that consists of not only seismic but also  
22 aseismic faults and discuss its two distinct implications. First, with the aid  
23 of a digital elevation model (DEM) and pre-existing geological and aftershock  
24 distribution data, we demonstrate that the InSAR data cannot be explained  
25 unless we introduce aseismic faults, and that the aseismic slip contributes to  
26 local topographic growth. Second, we test an emerging hypothesis that aseis-  
27 mic fault motion drives earthquake swarms, by employing detailed hypocenter  
28 data (Vidale and Shearer, 2006; Lohman and McGuire, 2007). Aseismic slip  
29 has been documented only in well-developed faults such as oceanic subduc-  
30 tion zones (e.g., Heki et al., 1997; Thatcher, 2001), and large scale continental  
31 transform faults (e.g., Rosen et al., 1998; Bürgman et al., 2000b; Fielding et  
32 al., 2004; Furuya and Satyabala, 2008). Although there are no well-developed  
33 faults, the Onikobe area is characterized by very high heat flow and hydrother-  
34 mal activities, which is preferable for the aseismic slip as demonstrated by  
35 some recent studies (McGuire et al., 2005; Vidale and Shearer, 2006; Lohman  
36 and McGuire, 2007). Our study verifies that aseismic slips can also occur in  
37 undeveloped fault under particular conditions.

## 38 **2 Observation Results and Fault Modeling**

39 InSAR images can detect mm to cm order changes in radar line-of-sight (LOS)  
40 through differential measurement of the phase component of temporally sep-  
41 arated SAR signals (e.g., Massonnet and Feigl, 1998; Bürgmann et al., 2000a;  
42 Hanssen, 2001). In this study, we used L-band (wavelength: 23.6 cm) JERS

43 data to overcome interferometric coherence loss because the studied area is  
 44 densely vegetated. Fig. 3 shows the three interferograms with good coherence  
 45 created from six independent acquisitions. To suppress atmospheric noise and  
 46 to evaluate measurement errors, we averaged those three independent inter-  
 47 ferograms (Fig. 4a) and defined the standard deviation  $\sigma$  for each pixel of the  
 48 averaged interferogram (Fig. 4d) (e.g., Goumelen and Amelung, 2005; Furuya  
 49 et al., 2007) by the following equation:

$$50 \quad \sigma(j) = \sqrt{\frac{\sum_{i=1}^3 (X_{avr}(j) - X_i(j))^2}{3 - 1}} \quad (1)$$

51 where  $j$  is the number of pixel,  $X_{avr}(j)$  and  $X_i(j)$  stand for the phase of  
 52 the averaged and the  $i$ -th interferograms, respectively. The denominator is 2  
 53 considering the unbiasedness. Our aim is to construct a fault model which can  
 54 explain the averaged interferogram (Fig.4a) within the standard deviation at  
 55 each pixel (Fig.4d).

56 Fig. 4a is characterized by the following three distinct signals. First, the largest  
 57 signal is observed in an inverted triangle-shaped area to the north of the  
 58 Onikobe caldera, where the radar LOS distance decreases by 14–18 cm around  
 59 the Torage (TRG) area (Fig. 1). Particularly remarkable is the very steep  
 60 gradient in  $\Delta$ LOS at the eastern and western margin of this area, which reaches  
 61 10 cm/km (equivalent to a strain of  $10^{-4}$ ) to locally 20 cm/km on both sides  
 62 (Fig. 5 top). Second, a broad positive  $\Delta$ LOS up to 5 cm is observed in the  
 63 northeastern part of the Onikobe caldera. Finally, a negative  $\Delta$ LOS area is  
 64 found to the south of the TRG area, where no earthquakes larger than M4.6  
 65 took place; this signal is robust in view of the two independent interferograms  
 66 (Figs. 3b and 3c). It was concluded that all ground deformations occurred

67 during the earthquake swarm event because no deformation signal could be  
68 detected in the interferograms before and after this event (Fig. 6).

69 Based on the focal mechanisms of large earthquakes and aftershocks, Umino  
70 et al.(1998) proposed a fault model that consists of three faults; we denote  
71 Umino et al's three faults as U1, U2, and U3 (Table 1). To represent the four  
72 largest earthquakes (Fig. 1), Umino et al. (1998) put U1 for two consecutive  
73 M5.9 and M5.4 events on Aug 11, U2 for the M5.7 event on Aug 11, and U3  
74 for the M5.0 event on Aug 13. Fig. 4b shows the calculated  $\Delta$ LOS based on  
75 Umino et al's model; we used the elastic dislocation model (Okada, 1992) to  
76 compute the  $\Delta$ LOS. Fig. 4e shows the root mean square (RMS) of the misfit  
77 between Figs. 4a and 4b, which can be defined as follows:

$$78 \quad RMS(j) = \sqrt{(X_{avr}(j) - X_s(j))^2} \quad (2)$$

79 where  $j$  is the number of pixel,  $X_{avr}(j)$  and  $X_s(j)$  stand for the phase of the  
80 averaged and the synthetic interferograms, respectively. Fig. 4e shows large  
81 discrepancies to the east and the west of the TRG area, because this fault  
82 model cannot explain the steep gradient in  $\Delta$ LOS noted above. Even if we  
83 considered a heterogeneous slip distribution on U1, we could not explain the  
84 steep gradient in  $\Delta$ LOS (Supplemental Fig. S1) not only because U1 is too  
85 deep (Table 1) to cause such localized signals but also because we assume a  
86 plane surface for the slip distribution. U2 and U3 are too far to affect the  
87 observed steep gradient in  $\Delta$ LOS. Also it is unlikely that heterogeneities in  
88 elastic properties, if they exist, make such very steep gradient in  $\Delta$ LOS. Thus  
89 we are led to prescribe two reverse faults at the western and eastern margins of  
90 the TRG area, which we hereafter denote F4 and F5. We cannot use seismicity  
91 to estimate the geometry of F4 and F5 because few earthquakes occurred

92 around these faults (Fig. 1). Instead, when comparing Fig.4a and 4c, the 2-  
93 dimensional pattern of  $\Delta$ LOS tightly constrains the geometry and location of  
94 these faults.

95 It is unrealistic to constrain all the fault geometries only from seismicities  
96 and faults on the surface, as the studied area is highly fractured due to past  
97 caldera collapse and each fault is not exposed on the surface as noted above.  
98 This is also evidenced by the mismatch between aftershock locations and the  
99 geometry of the faults U1–U3. The essence of our modelling strategy is to  
100 explain the InSAR data, using minimum number of fault planes. We named  
101 each fault of our original model as F1 F2... to clearly distinguish our model  
102 from Umino’s fault model U1–U3. Considering from different types of focal  
103 mechanisms (Fig.2), at the very least, we have to introduce two faults F1 and  
104 F2; F1 corresponds to M5.9 and M5.4, and F2 represent M5.7 earthquakes.  
105 Meanwhile, comparing Figs. 4a and 4b, we cannot find any InSAR signals  
106 associated with the M5.0 earthquake that led Umino et al to propose their U3,  
107 which is presumably because the moment release is small (Table 1). Therefore,  
108 we did not take this earthquake into account. Considering the good accuracy  
109 of hypocenter determination, the negative  $\Delta$ LOS to the south of the TRG  
110 area is unlikely to be caused by the M5.0 event and therefore it needs to be  
111 explained by another source F3, which is not a repositioned model of U3 but  
112 totally new fault detected solely by InSAR as well as F4 and F5. It should  
113 be noted that this signal is very robust in light of short wavelength and small  
114 standard deviation  $\sigma$  (Fig.4d). We discuss the geophysical implication of F3  
115 in Section 3.2. Thus, we introduce five faults as the minimum fault number  
116 to account for the InSAR and seismological data. We stressed again that few  
117 earthquakes occurred in and around the faults F4 and F5, and that there are

118 no specific earthquakes correspond to the faults F3–F5 (Figs. 1 and 2).

119 We first found plausible ranges of each fault parameter by a trial-and-error for-  
120 ward modeling approach, and then adopted a grid-search approach to obtain  
121 the fault parameters in our model (Table 2). Although non-linear inversion  
122 approach is often taken to constrain nine parameters for a uniform slip model  
123 (e.g., Aoki et al.1999), it is unrealistic to precisely determine the 45 indepen-  
124 dent parameters by any non-linear inversion methods. Also, any non-linear  
125 inversion methods need very good initial estimates predetermined by forward  
126 modeling. We think that if the initial estimate explains the data (Fig.4a)  
127 within the error level (Fig.4d) it should be very close to the true solution,  
128 and that our approach is a realistic and reliable way at the moment. Con-  
129 sidering the complex crustal structure in this area, we do not rely absolutely  
130 on the fault parameters of U1 and U2 in making our model. Actually, we  
131 could not explain the InSAR data when we incorporated U1 and U2 in our  
132 model without any modifications. We used the fault parameters of U1 and U2  
133 as the initial estimates of F1 and F2. Because of the strong dependence of  
134  $\Delta$ LOS on each parameter, the acceptable ranges obtained in our model are  
135 quite narrow, especially for the fault location. The synthetic  $\Delta$ LOS calculated  
136 from our preferred model and its RMS misfit are shown in Figs. 4c and 4f,  
137 respectively. The RMS misfits are largely within the standard deviation of the  
138 observed data (Figs. 4d and 4f). However, we can identify a spotty but signif-  
139 icant misfit in Fig. 4f. We believe that the spotty misfit is caused by a local  
140 small landslide that was probably triggered during the swarm event because  
141 (1) the area closely matches the local landslide morphology (H. Yarai and T.  
142 Ozawa, personal communication, 2008) and (2) the sign of  $\Delta$ LOS is consistent  
143 with the direction of the landslide.

144 It should be noted that the faults F4 and F5 are located within gaps in the  
145 swarm seismicity (Fig. 1), which would be explained by extraordinary high  
146 temperature to the east and west of the TRG areas estimated from the bore  
147 hole data (Tamanyu et al., 1996), low S-wave velocity anomaly, and anoma-  
148 lously high S-wave attenuation (Onodera et al., 1998). Actually, we also ob-  
149 served few seismicities in the southern part of the Onikobe caldera where  
150 geothermal gradients far exceed  $200\text{C}^\circ/\text{km}$  and a geothermal power plant ex-  
151 ists (PP in Fig.1). The depth of very few earthquakes in the vicinity of F4  
152 and F5 are far deeper than the inferred depth ranges of F4 (0.5 km to 4.5 km)  
153 and F5 (0.6 km to 6.6 km), and the magnitudes of those earthquakes are very  
154 small ( $M < 3.0$ ). Only one medium earthquake (M4.7) occurred close to the  
155 southern tip of F5, but it accounted for only  $\sim 20\%$  of the slip amount of F5.  
156 Hence, F4 and F5 clearly represent faults that slipped aseismically, although  
157 the exact timing of the slip remains uncertain because of poor time resolution  
158 of the InSAR data.

### 159 **3 Discussion**

#### 160 *3.1 Insights Into Topographic Growth*

161 Cumulative crustal deformation due to repetitive fault motion and surface  
162 processes over a long time-scale are known to produce topographic expressions  
163 (e.g., Burbank and Anderson, 2001; Hallet and Molnar, 2001). By combining  
164 a DEM and the InSAR technique, we have found that the TRG area is an  
165 intriguing example of the coupling between tectonics and surface processes.

166 Fig. 5 (top) shows the cross-sectional profile of the surface topography and

167 the  $\Delta$ LOS along a track across the TRG area; this figure shows that the  
168 location of abrupt changes in  $\Delta$ LOS due to F4 and F5 coincides with that  
169 of the sharp ridges at the western and eastern margins of the TRG area.  
170 While the subsurface reverse fault motion on F4 and F5 does contribute to  
171 the growth of the sharp ridge, the surface processes, especially river incision,  
172 also affect topographic evolution because of the high annual rainfall in this  
173 region. Within the region bounded by the sharp ridge (indicated by a black  
174 line), there are two rivers running in deep V-shaped valleys (Fig. 5 top and  
175 middle), which should have denudated the inner flank of the sharp ridge. The  
176 combination of the steep and localized deformations due to the slips on F4  
177 and F5 and the river incision process has driven the topographic evolution of  
178 the sharp ridge. We also observe a domal topographic high above the central  
179 part of F1, where the ground displacement toward satellite culminates (Fig. 5  
180 top and Fig. 4c). River drainage patterns are widely used as good geomorphic  
181 markers of crustal deformation (e.g., Burbank and Anderson, 2001; Hallet  
182 and Molnar, 2001); Fig. 5 (middle) clearly shows that the two rivers (red  
183 lines) change their course around the domal topographic high, which suggests  
184 that the domal high grows rapidly at a rate comparable to or faster than the  
185 river incision rate. Our model explains this uplift pattern well in terms of the  
186 superposition of surface uplift due to F1, F4, and F5. The contributions of F4  
187 and F5 are large because the domal high is located on the hanging-wall side  
188 of both faults.

189 The very steep faults, F4 and F5, would have originated in the Mio-Pliocene  
190 caldera collapse, as revealed by detailed geological surveys (Ito et al., 1989;  
191 Yoshida, 2001). Although most surface topographies related to the caldera  
192 formation are now buried underneath subsequent volcanic sediments, many

193 subsurface structures have remained and currently serve as pre-existing weak-  
194 nesses under the present regional tectonic regime. Umino et al. (1998) have  
195 already pointed out the importance of old subsurface caldera structures as  
196 pre-existing weaknesses for earthquake rupture; however, this study demon-  
197 strates that the old subsurface caldera structures can also generate aseismic  
198 slip, such as those found on F4 and F5, and contribute to the topographic  
199 growth.

### 200 *3.2 Aseismic Fault Drives Earthquake Swarm?*

201 The stress triggering mechanism has been successfully exploited to account  
202 for the spatiotemporal evolution of earthquake sequences (e.g., Stein, 1999;  
203 Scholz, 2002). For earthquake swarm episodes around volcanic or geothermal  
204 areas, however, Vidale and Shearer (2006) and Vidale et al. (2006) have sug-  
205 gested that pore fluid pressure fluctuation and/or aseismic deformation would  
206 be more likely drivers rather than the stress triggering mechanism. Lohman  
207 and McGuire (2007) proposed an aseismic fault model to account for the In-  
208 SAR data associated with the Obsidian Buttes swarm in 2005; their model  
209 supports the hypothesis that aseismic creep drives some earthquake swarms.

210 Among the proposed fault sources, F3, F4, and F5 do not accompany large  
211 earthquakes with equivalent moment magnitudes of these faults (Table 2)  
212 and thus we conclude that these faults slip primarily aseismically. While F4  
213 and F5 reside in seismicity gaps, we observed numerous small ( $M < 4.6$ )  
214 earthquakes around F3 (Fig. 1). In contrast to the aftershocks around the  
215 fault F1, we confirmed that those earthquakes around F3 did not indicate  
216 mainshock-aftershock sequences (Fig. 7a). Despite the small magnitudes of the

217 earthquakes, significant deformation was detected by InSAR (Figs. 3 and 4a),  
218 and the moment magnitude of F3 far exceeds that of the nearby earthquakes.  
219 These observations thus support the emerging model that shallow aseismic  
220 slip drives seismic swarms.

221 Although the studied area lies close to an active volcano, Mt. Kurikoma (Fig.  
222 1), there is no evidence of magma intrusion during the 1996 Onikobe event, un-  
223 like other reports, for example, on the eastern Izu-peninsula (Aoki et al., 1999)  
224 and near Lake Tahoe (Smith et al., 2004). As another swarm mechanism, pore  
225 pressure perturbation cannot be precluded because it can be caused by water  
226 as well. The seismic tomography indeed indicates abundant water in the up-  
227 permost crust of the Onikobe area (Nakajima and Hasegawa, 2003). It should  
228 be noted, however, that such a water-rich environment is also favorable for  
229 aseismic slip. In addition, as evidenced by low  $V_s$  anomaly over 10% (Onodera  
230 et al., 1998) and a very high geothermal gradient (100–150 C°/km, or higher)  
231 (Tanaka et al., 1999; Tamanyu et al., 1996), the Onikobe area is clearly under  
232 high temperature, which suggests that the brittle-ductile transition zone is  
233 shallow and that the aseismic slip on F3 is likely to occur across the transi-  
234 tion zone. Considering that there is no direct observation of anomalous water  
235 diffusion during the swarm, we speculate that abundant geothermal fluid does  
236 not directly drive swarm events but assists aseismic slip. We need to check if  
237 aseismic deformation always occurs for the other swarm events as well.

238 To quantify the amount of aseismic slip on F3, we plotted the depth ranges of  
239 the fault slip and seismicity just below and above the fault F1 (Fig.7b) and  
240 F3 (Fig.7c), respectively. The localized and robust signal detected by InSAR  
241 near F3 (Fig. 4) requires the fault slip on F3 limited to shallow depth. Figure  
242 7b indicates that the fault slip on F3 is much shallower than that of seismicity

243 unlike F1 (Fig.7c), which demonstrated that almost all the fault slip on F3  
244 is aseismic. Considering observation errors of the moment magnitudes and  
245 hypocentral depths, the aseismic slip on F3 is not obvious. However, such a  
246 very shallow earthquake that accounts for the remarkable InSAR signal around  
247 F3 is unlikely to occur because of low crustal strength. Thus we conclude that  
248 the aseismic slip on F3 is highly likely. Further discussion is difficult because  
249 the rock type distribution is very complex and F3 locates in the marginal area  
250 of very high geothermal gradient in the southern part of the Onikobe caldera  
251 as evidenced by the geothermal power plant, geysers, and few seismicities  
252 (Fig.1).

### 253 **Acknowledgments**

254 The original JERS-1 SAR data are the copyright of METI/JAXA, Japan.  
255 The hypocenter data have been provided by JMA. This work was supported  
256 by a Grant-in-Aid for Scientific Research (B), 19340123. We thank Takeyoshi  
257 Yoshida, Kosuke Heki and Yukiotoshi Fukahata for their helpful comments and  
258 discussions. We also thank C.P. Jaupart and two anonymous reviewers for  
259 valuable comments.

### 260 **References**

- 261 [1] Aki, K., Richards, P.G., 1980. Quantitative seismology. Freeman, San Francisco.
- 262 [2] Aoki, S., Furuya, M., Kobayashi, S., Okubo, S., 2002. Co-seismic crustal  
263 deformation of the 1996 Onikobe earthquakes, Japan, detected by InSAR. EOS  
264 Trans. AGU. 83, (47), Fall Meet. Suppl. F362.
- 265 [3] Aoki, Y., Segall, P., Kato, T., Cervelli, P., Shimada. S., 1999. Imaging magma

- 266 transport during the 1997 seismic swarm off the Izu peninsula, Japan. *Science*  
267 286, 927–930.
- 268 [4] Burbank, D.W., Anderson, R.S., 2001. *Tectonic geomorphology*. Blackwell  
269 Science, Oxford, UK.
- 270 [5] Bürgmann, R., Rosen P.A., Fielding, E.J., 2000a. Synthetic aperture radar  
271 interferometry to measure Earth’s surface topography and its deformation.  
272 *Annu. Rev. Earth Planet Sci.* 28, 169–209.
- 273 [6] Bürgmann, R., Schumidt D., Nadeau, R.M., d’Alessio, M., Fielding, E.,  
274 Manaker, D., McEvilly, T.V., Murray, M.H., 2000b. Earthquake potential along  
275 the Northern Hayward Fault, California. *Science* 289, 1178–1182.
- 276 [7] Fielding, E. J., Wright, T.J., Muller, J., Parsons, B.E., 2004. Aseismic  
277 deformation of a fold-and-thrust belt imaged by synthetic aperture radar  
278 interferometry near Shahdad, southeast Iran. *Geology* 32, 577–580, doi:  
279 10.1130/G20452.1.
- 280 [8] Furuya, M., Mueller, K., Wahr J., 2007. Active salt tectonics in the Needles  
281 District, Canyonlands (Utah) as detected by interferometric synthetic aperture  
282 radar and point target analysis: 1992–2002. *J. Geophys. Res.* 112, B06418, doi:  
283 10.1029/2006JB004302.
- 284 [9] Furuya, M., Satyabala, S. P., 2008. Slow earthquake in Afghanistan detected  
285 by InSAR, *Geophys. Res. Lett.*, 35, L06309, doi:10.1029/2007GL033049.
- 286 [10] Geological Survey of Japan (ed.) (2004) *Digital Geological Map of Japan*  
287 1:200,000, Tohoku. Digital Geoscience Map G20-3, Geological Survey of Japan,  
288 AIST
- 289 [11] Gournelen, N., Amelung, F., 2005. Postseismic mantle relaxation in the central  
290 Nevada seismic belt. *Science* 310, 1473–1476.

- 291 [12] Hallet, B., Molnar, P., 2001. Distorted drainage basins as markers of crustal  
292 strain east of the Himalaya. *J. Geophys. Res.* 106, 13697–13709.
- 293 [13] Hanssen, R. F., 2001. Radar interferometry -Data Interpretation and Error  
294 Analysis-. Kluwer Academic Publishers, Dordrecht, Netherlands.
- 295 [14] Heki, K., Miyazaki, S., Tsuji, H., 1997. Silent fault slip following an interplate  
296 thrust earthquake at the Japan Trench. *Nature* 386, 595–598.
- 297 [15] Ito, T., Utada M., Okuyama, T., 1989. Mio-Pliocene calderas in the backbone  
298 region in northeast Japan (in Japanese with English abstract). *Mem. Geol. Soc.*  
299 *Japan* 32, 409–429.
- 300 [16] Kanamori, H., 1977. The energy release in great earthquakes. *J. Geophys. Res.*  
301 82, 2981-2987.
- 302 [17] Lohman, R.B., McGuire, J.J., 2007. Earthquake swarms driven by aseismic  
303 creep in the Salton Trough, California. *J. Geophys. Res.* 112, B04405, doi:  
304 10.1029/2006JB004596.
- 305 [18] Massonnet, D., Feigl, K.L., 1998. Radar interferometry and its application to  
306 changes in the Earth's surface. *Rev. Geophys.* 36, 441–500.
- 307 [19] McGuire, J.J., Boettcher, M.S., Jordan, T.H., 2005. Foreshock sequences and  
308 short-term earthquake predictability on east pacific rise transform faults.  
309 *Nature.* 434, 457–461.
- 310 [20] Nakajima, J., Hasegawa, A., 2003. Tomographic imaging of seismic velocity  
311 structure in and around the Onikobe volcanic area, northeastern Japan:  
312 Implications for fluid distribution. *J. Volcanol. Geotherm. Res.* 127, 1–18.
- 313 [21] Okada, Y., 1992. Internal deformation due to the shear and tensile faults in a  
314 half-space. *Bull. Seismo. Soc. America* 82, 1018–1042.

- 315 [22] Okada, T., Umino, N., Ito, Y., Matsuzawa, T., Hori, S., Kono, T., Nida, K.,  
316 Hasegawa, A., 2001. Source process of moderate earthquakes that occurred in  
317 the upper crust of NE Japan (in Japanese with English abstract). *Bull. Earthq.*  
318 *Res. Inst. Univ. Tokyo* 76, 61–74.
- 319 [23] Onodera, M., Horiuchi, S., Hasegawa, A., 1998. Three-dimensional seismic  
320 velocity structure in and around the focal area of the 1996 Onikobe earthquake  
321 based on  $V_p/V_s$  inversion (in Japanese with English abstract). *J. Seismol. Soc.*  
322 *Jpn.* 51, 265–279.
- 323 [24] Rosen, P., Werner, C., Fielding, E., Hensley, S., Buckley, S., Vincent, P.,  
324 1998. Aseismic creep along the San Andreas Fault northwest of Parkfield, CA  
325 measured by radar interferometry. *Geophys. Res. Lett.* 25, 825–828.
- 326 [25] Scholz, C. H., 2002. *The Mechanics of Earthquakes and Faulting*. Cambridge  
327 University Press, New York.
- 328 [26] Smith, K. D., von Seggern, D., Blewitt, G., Preston, L., Anderson, J.G.,  
329 Wernicke, B.P., Davis, J.L., 2004. Evidence for deep magma injection beneath  
330 Lake Tahoe, Nevada-California. *Science* 305, 1277–1280.
- 331 [27] Stein, R. S., 1999. The role of stress transfer in earthquake occurrence. *Nature*  
332 402, 605–609.
- 333 [28] Tamanyu, S., Nomura, K., Yoshizawa, M., 1996. Deep subsurface temperature  
334 distribution patterns estimated from temperature logging data: Examples of  
335 14 major geothermal field in Japan (in Japanese with English abstract). *Bull.*  
336 *Geol. Surv. Japan* 47, (10), 485–548.
- 337 [29] Tanaka, A., Yano, Y., Sasada, M., Okubo, Y., Umeda, K., Nakatsuka, N., Akita,  
338 F., 1999. Compilation of thermal gradient data in Japan on the basis of the  
339 temperatures in boreholes (in Japanese with English abstract). *Bull. Geol. Surv.*  
340 *Japan* 50, (7), 457–487.

- 341 [30] Thatcher, W., 2001. Silent slip on the Cascadia subduction interface. *Science*  
342 292, 1495–1496.
- 343 [31] Umino, N., Matsuzawa, T., Hori, S., Nakamura, A., Yamamoto, A., Hasegawa,  
344 A., Yoshida, T., 1998. 1996 Onikobe earthquakes and their relation to crustal  
345 structure (in Japanese with English abstract). *J. Seismol. Soc. Jpn.* 51, 253–264.
- 346 [32] Vidale, J.E., Shearer, P.M., 2006. A survey of 71 earthquake bursts  
347 across southern California: Exploring the role of pore fluid pressure  
348 fluctuations and aseismic slip as drivers. *J. Geophys. Res.* 111, B05312, doi:  
349 10.1029/2005JB004034.
- 350 [33] Vidale, J.E., Boyle, K.L., Shearer, P.M., 2006. Crustal earthquake bursts in  
351 California and Japan: Their patterns and relation to volcanoes. *Geophys. Res.*  
352 *Lett.* 33, L20313, doi: 10.1029/2006GL027723.
- 353 [34] Yarai, H., Murakami, M., Tobita, M., Nakagawa, H., Fujiwara, S., 2002. Crustal  
354 deformation associated with earthquakes occurred in north Akita prefecture on  
355 August 11, 1996: from JERS-1 SAR interferometry (in Japanese). Programme  
356 and abstracts. *Seismol. Soc. Jpn.* 2002 Fall Meeting, P-202.
- 357 [35] Yoshida, T., 2001. The evolution of arc magmatism in the NE Honshu arc,  
358 Japan. *Sci. Rep. Tohoku Univ.* 36, 131–149.

## 359 **Figure Captions**

360 **Fig. 1.** Tectonic map of the 1996 Onikobe earthquake swarm area. The circles  
361 indicate the hypocenters given by JMA (11 Aug. 1996 – 30 Sept. 1996). The  
362 magnitude and depth of the earthquakes are indicated by radius and color, re-  
363 spectively. The major earthquakes are shown by different symbols: M5.9 (star,  
364 11 Aug.), M5.4 (square, 11 Aug.), M5.7 (diamond, 11 Aug.), M5.0 (inverted  
365 triangle, 13 Aug.). The red diamonds indicate major hot springs, geysers,

366 and fumaroles. The large red diamond denoted by PP indicates a geothermal  
367 power plant. TRG: Mt. Torage, KRK: Mt. Kurikoma (active volcano), ARD:  
368 Mt. Arao (active volcano, and the center of the Onikobe caldera). The white  
369 broken lines show the location of Fig. 5. The rectangles with solid lines indi-  
370 cate the surface projections of the aseismic faults (F4 and F5 in Table 2). The  
371 rectangle with white dotted line indicates the surface projection of another  
372 aseismic fault (F3 in Table 2).

373 **Fig. 2.** Focal mechanisms of major earthquakes superposed on the geologic  
374 map (Geological Survey of Japan, 2004). The focal solutions (lower hemisphere  
375 projection) are given by Umino et al.(1998). We added two large earthquakes  
376 occurred on 1976 and 1985 for reference. Legend of the geologic map is simpli-  
377 fied. The white triangles indicate main landmarks. TRG: Mt. Torage, KRK:  
378 Mt. Kurikoma, ARD: Mt. Arao. The solid lines indicate known faults and the  
379 broken lines denote concealed faults. The red circle indicates Onikobe Caldera  
380 (after Yoshida, 2001). Note that both focal mechanisms and geologic map  
381 reflect highly complex crustal structure.

382 **Fig. 3.** Interferograms acquired from three independent periods. a) 23 Jul.  
383 1995 - 5 Oct. 1996, b) 12 Apr. 1996 - 19 Dec. 1997, c) 9 Jul. 1996 - 13  
384 Jun. 1998. Data were taken along descending path 64 and rows 235 to 236.  
385 To remove the topographic fringes, we used a digital elevation map with a  
386 resolution of 50 m provided by the Geographical Survey Institute, Japan.

387 **Fig. 4.** Comparison between observed and synthetic  $\Delta$ LOS. Positive (nega-  
388 tive)  $\Delta$ LOS stands for an increase (decrease) in the LOS distance. a) Observed  
389  $\Delta$ LOS. b) and c) are the synthetic  $\Delta$ LOS calculated from the fault model of  
390 Umino et al. (1998) and this study, respectively. d) Standard deviation of a).

391 See text for details. e) Root mean square (RMS) misfit between a) and b).  
392 f) RMS misfit between a) and c). The white frames and vectors indicate the  
393 fault surface and slip vectors projected onto the surface, respectively.

394 **Fig. 5.** Spatial relationship between  $\Delta$ LOS, topography, and inferred aseismic  
395 faults. The location is indicated in Fig. 1. Top:  $\Delta$ LOS (blue) and altitude (red)  
396 along the white line in the middle figure. Middle: 3D view of the Torage area  
397 from the north.  $\Delta$ LOS value is draped onto the topography. The triangle  
398 indicates the summit of Mt. Torage (1432.9 m). The marked negative  $\Delta$ LOS  
399 area is surrounded by a sharp ridge (black line). The domal topographic high  
400 inside the sharp ridge shows good spatial correlation with the negative  $\Delta$ LOS  
401 area. The red lines indicate major rivers flowing in deep valleys. Bottom: 3D  
402 view of the inferred high dip-angle aseismic faults (F4 and F5) running parallel  
403 to the sharp ridge.

404 **Fig. 6.** Interferograms obtained before and after the earthquake swarm. (a)  
405 12 Apr. 1996 - 9 Jul. 1996 (before), (b) 5 Oct. 1996 - 19 Dec. 1997 (after), (c)  
406 19 Dec. 1997 - 13 Jun. 1998 (after).

407 **Fig. 7.** (a) Time sequence of the earthquakes around F1 and F3 during 11-  
408 14 August 1996. The red and green crosses correspond to the earthquakes  
409 with those epicenters inside the surface projection of F1 and F3, respectively  
410 (Figs. 1 and 4c). The magnitudes are normalized by those of the largest earth-  
411 quake for both sequences. The green symbols do not indicate the mainshock-  
412 aftershock sequence unlike the red symbols. Depth distribution of earthquakes  
413 with those epicenters inside the surface projection of (b) F1 and (c) F3 are  
414 also plotted. Red bar in (b) and green bar in (c) indicate the depth range of  
415 the fault F1 and F3, respectively.

416 **Fig. S1.** Fault modeling considering slip distribution. (a) Observed  $\Delta$ LOS  
417 (Fig.4a). (b) Synthetic  $\Delta$ LOS based on distributed slip fault models, Um1 and  
418 Um2. The location and geometry of Um1 and Um2 are slightly modified from  
419 Umino et al.'s U1 and U2. Slip distribution on Um1 and Um2 are indicated in  
420 (c) and (d), respectively. Color indicates the amount of slip in meter. Bottom  
421 depth, length, width, dip, and strike of Um1 is 7.5 km, 10 km, 5 km, 45 degree,  
422 and 350 degree, respectively. Those for Um2 is 8.0 km, 11 km, 5 km, 90 degree,  
423 and 225 degree, respectively.

**Table 1.** Fault parameters estimated from the seismological data.

Fault	Longitude <sup>a</sup> (deg)	Latitude <sup>a</sup> (deg)	Length (km)	Width (km)	Depth <sup>a</sup> (km)	Dip <sup>b</sup> (deg)	Strike <sup>b</sup> (deg)	Rake <sup>b</sup> (deg)	Slip (cm)	Mw <sup>c</sup>
U1	140.627	38.899	10.0	8.2	7.5	45.0	350.0	90.0	60	6.15
U2	140.649	38.855	10.0	6.0	7.0	90.0	47.0	180.0	40	5.94
U3	140.576	38.800	5.0	3.0	8.0	50.0	49.0	120.0	40	5.54

Each value was scanned from Figure 9 in Umino et al. (1998). We also referred to Okada et al. (2001) while obtaining some parameters from Umino et al. (1998).

<sup>a</sup> The position is for the center of each fault plane.

<sup>b</sup> We adopted the convention defined by Aki and Richards (1980).

<sup>c</sup> Equivalent moment magnitude defined by Kanamori (1977).

**Table 2.** Fault parameters of our model and those acceptable ranges indicated by  $\pm$ .

Fault	Longitude <sup>a</sup> (deg)	Latitude <sup>a</sup> (deg)	Length (km)	Width (km)	Depth <sup>a</sup> (km)	Dip <sup>b</sup> (deg)	Strike <sup>b</sup> (deg)	Rake <sup>b</sup> (deg)	Slip (cm)	Mw <sup>c</sup>
F1	140.640 $\pm$ 0.003	38.905 $\pm$ 0.003	9.0 $\pm$ 0.5	5.3 $\pm$ 0.3	6.7 $\pm$ 0.3	40.0 $\pm$ 2.5	340.0 $\pm$ 5.0	110 $\pm$ 5	52 $\pm$ 3	5.95 $\pm$ 0.05
F2	140.650 $\pm$ 0.002	38.860 $\pm$ 0.002	7.8 $\pm$ 0.5	6.8 $\pm$ 0.2	5.5 $\pm$ 0.2	80.0 $\pm$ 2.5	47.0 $\pm$ 2.0	-169 $\pm$ 1	44 $\pm$ 3	5.93 $\pm$ 0.04
F3	140.648 $\pm$ 0.002	38.831 $\pm$ 0.003	5.8 $\pm$ 0.4	2.0 $\pm$ 0.2	2.1 $\pm$ 0.3	37.5 $\pm$ 2.5	12.5 $\pm$ 2.5	115 $\pm$ 3	30 $\pm$ 2	5.38 $\pm$ 0.07
F4	140.601 $\pm$ 0.001	38.909 $\pm$ 0.001	6.0 $\pm$ 0.5	4.0 $\pm$ 0.2	2.5 $\pm$ 0.1	86.0 $\pm$ 2.0	325.0 $\pm$ 2.5	80 $\pm$ 10	20 $\pm$ 2	5.48 $\pm$ 0.07
F5	140.663 $\pm$ 0.002	38.916 $\pm$ 0.002	5.0 $\pm$ 0.5	6.0 $\pm$ 0.2	3.6 $\pm$ 0.2	84.0 $\pm$ 2.0	21.0 $\pm$ 5.0	90 $\pm$ 10	20 $\pm$ 5	5.54 $\pm$ 0.11

<sup>a</sup> The position is for the center of each fault plane.

<sup>b</sup> We adopted the convention defined by Aki and Richards (1980).

<sup>c</sup> Equivalent moment magnitude defined by Kanamori (1977).

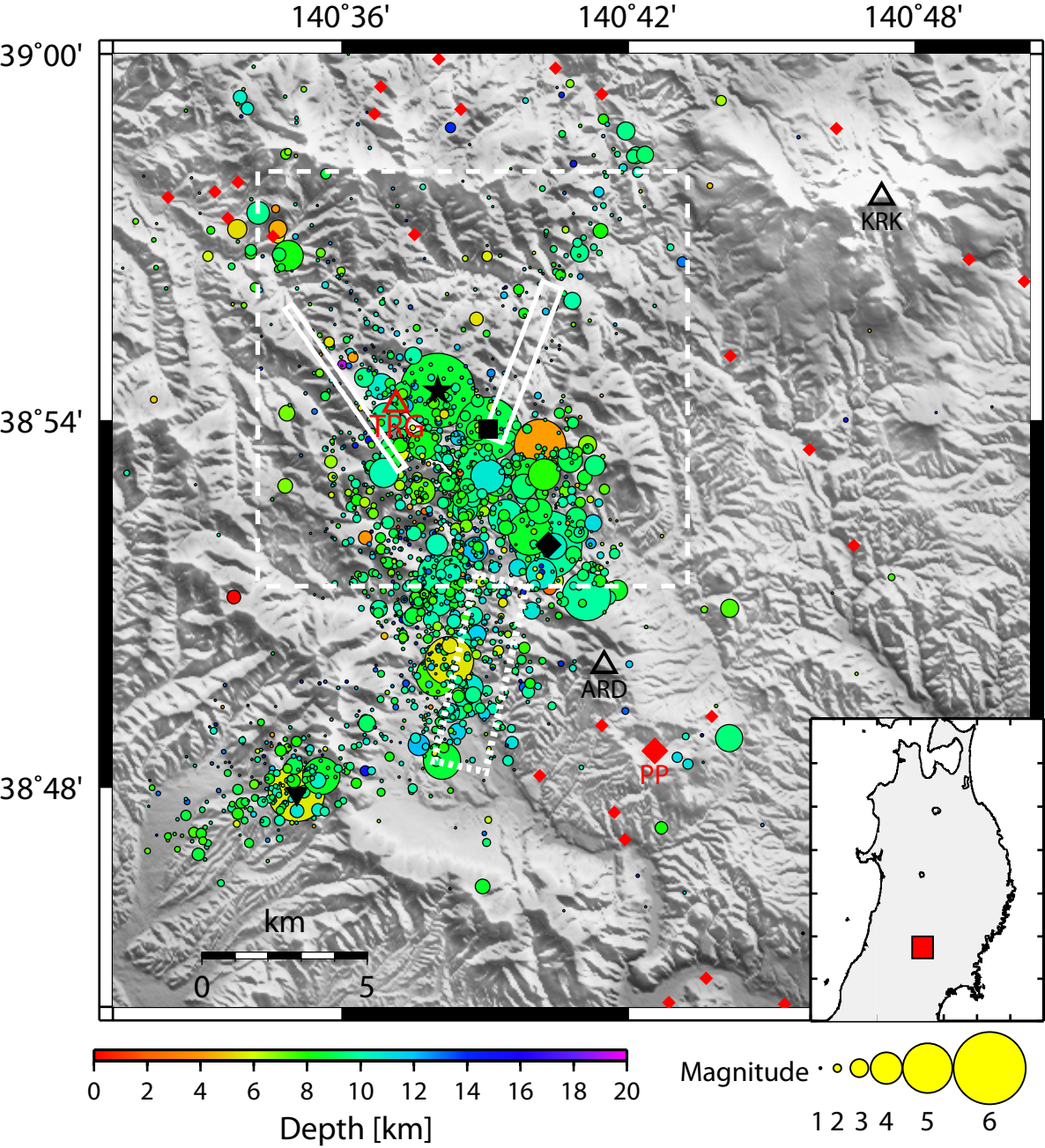


Fig.1

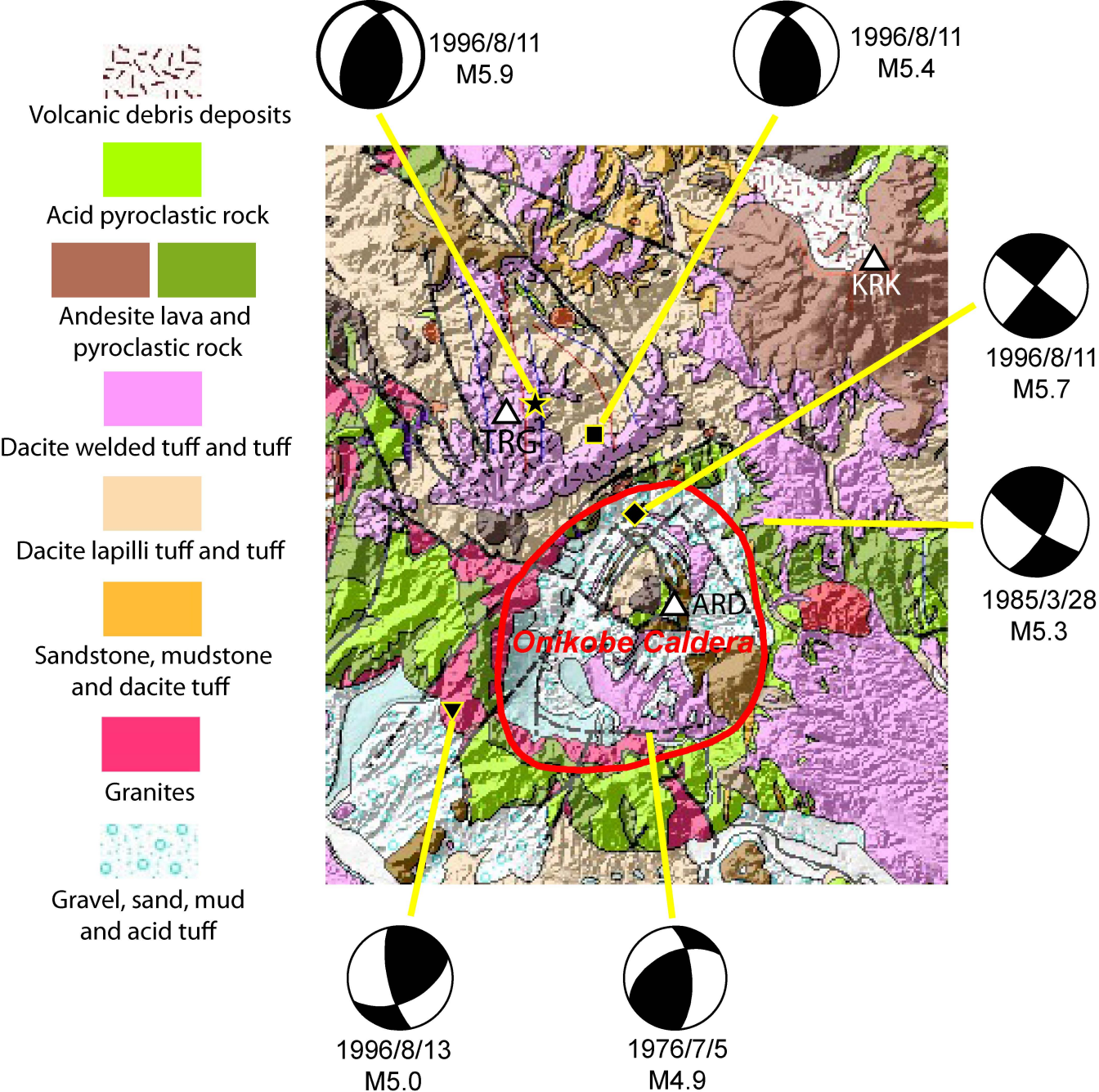
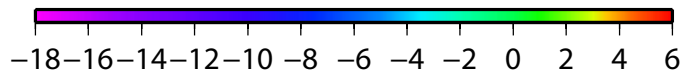
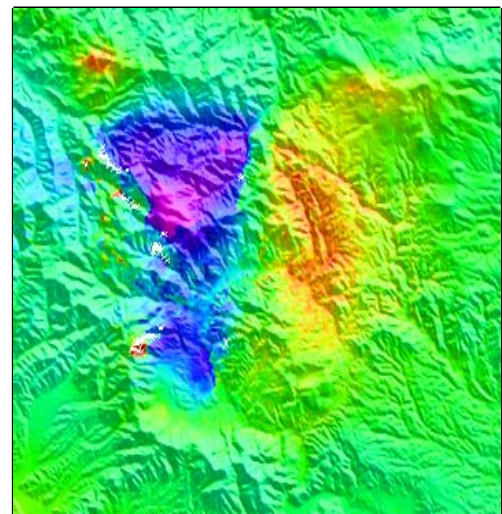
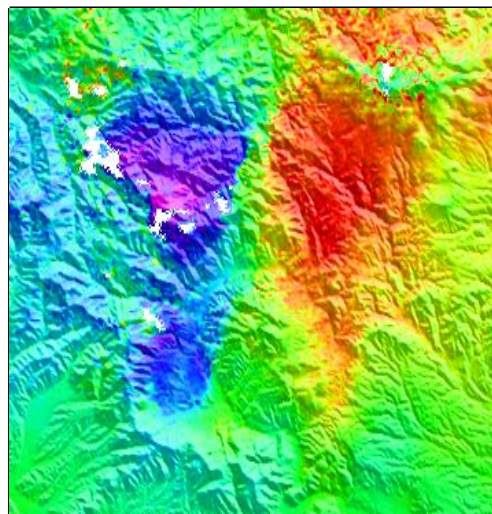
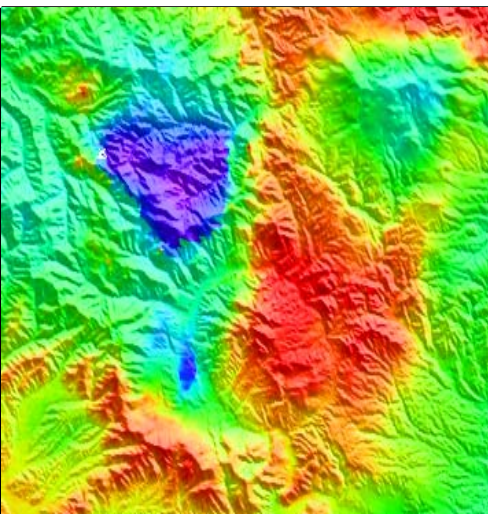


Fig.2

a) 23 Jul.1995 - 5 Oct. 1996

b) 12 Apr.1996 - 19 Dec. 1997

c) 9 Jul.1996 - 13 Jun. 1998



$\Delta$ LOS [cm]

Fig.3

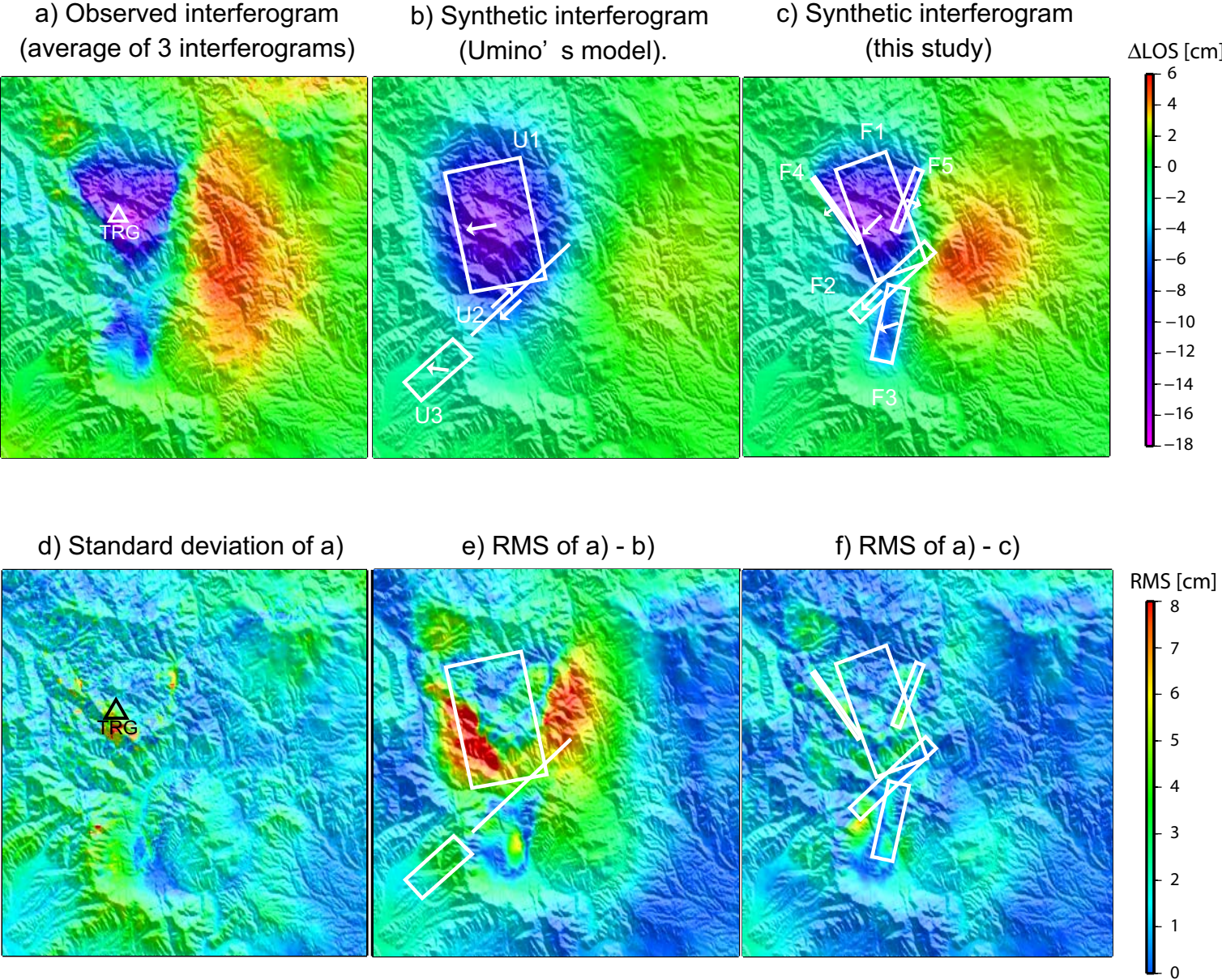
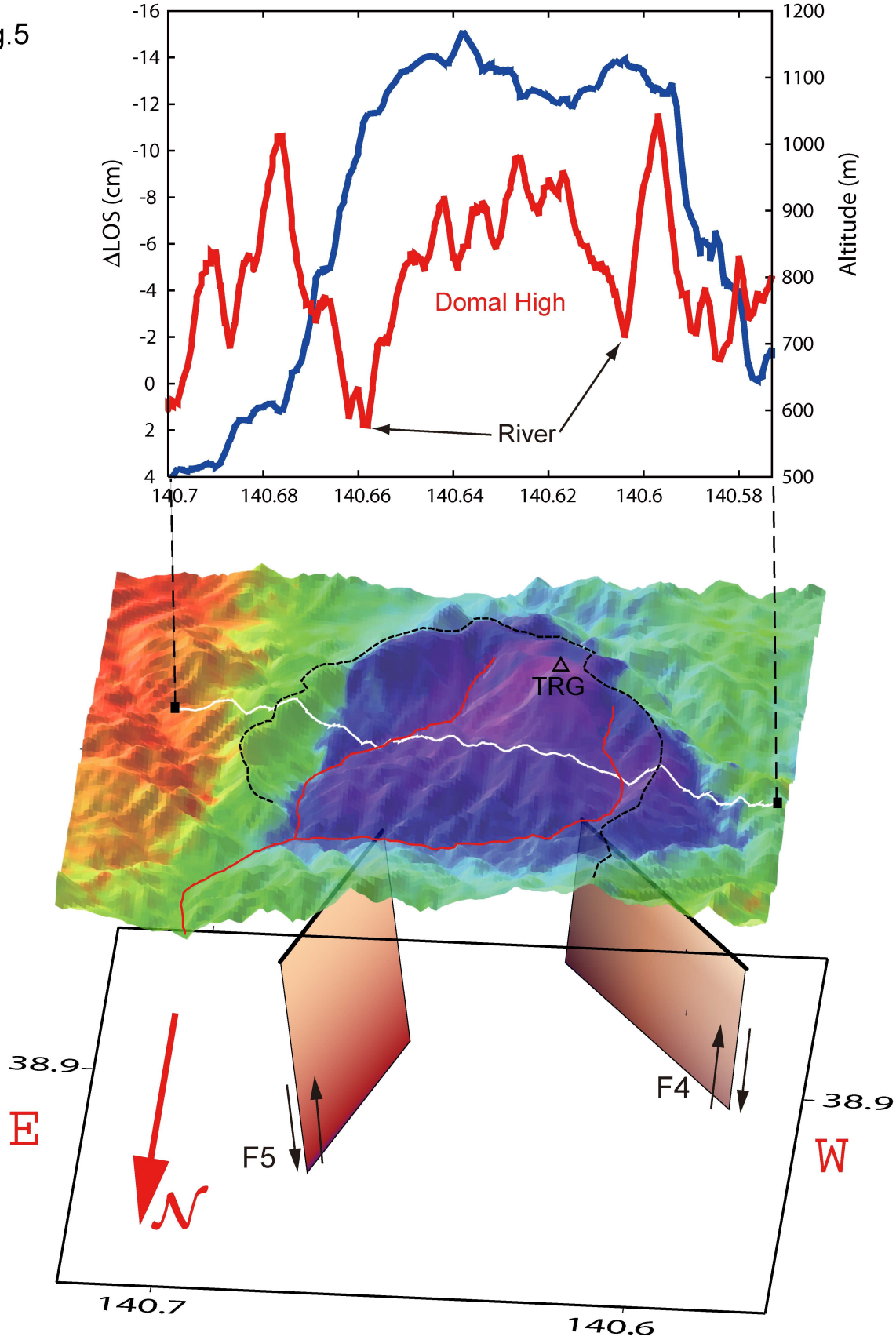


Fig.4

Fig.5



a) 12 Apr. 1996 - 9 Jul. 1996

b) 5 Oct. 1996 - 19 Dec. 1997

c) 19 Dec. 1997 - 13 Jun. 1998

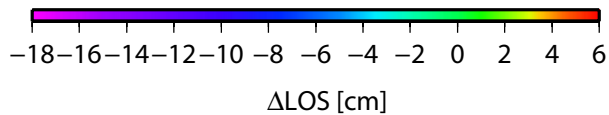
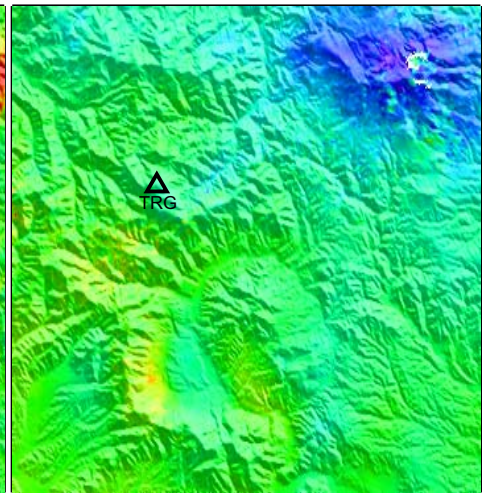
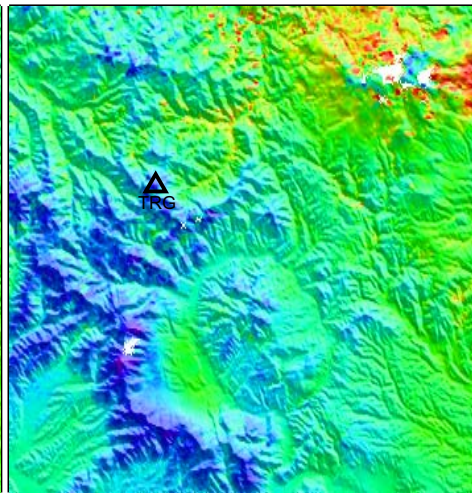
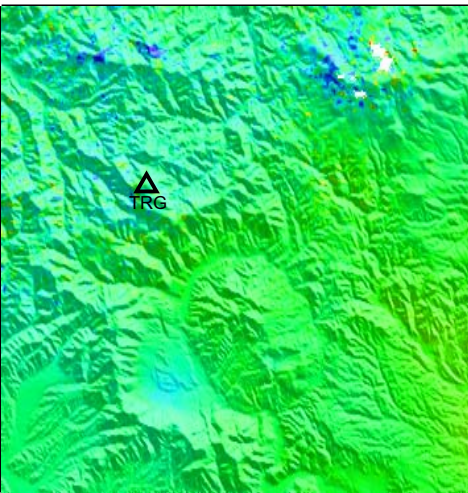


Fig.6

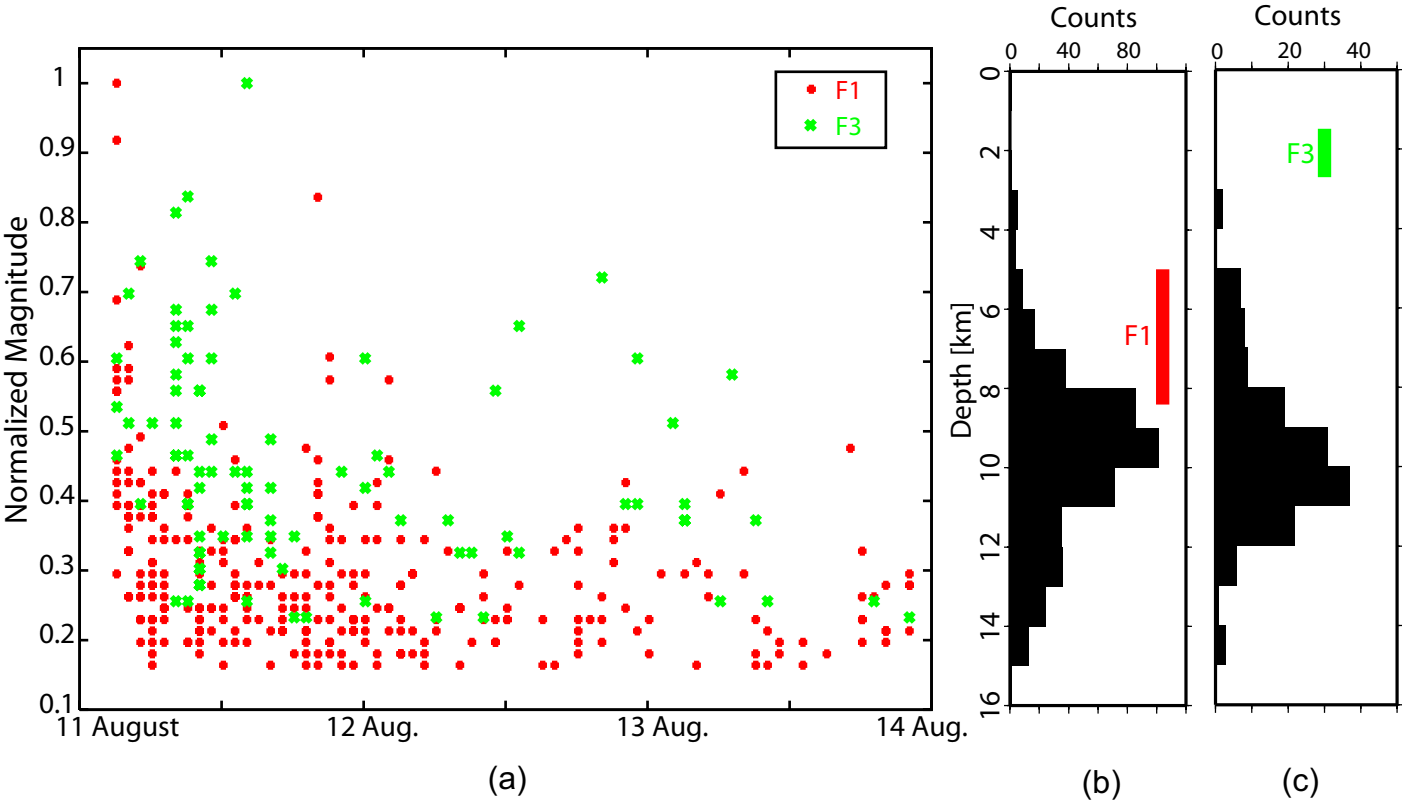


Fig. 7

